Proceedings of the ASME 2010 3rd Joint US-European Fluids Engineering Summer Meeting and 8th International Conference on Nanochannels, Microchannels, and Minichannels
FEDSM-ICNMM2010
August 1-5, 2010, Montreal, Canada

FEDSM-ICNMM2010-30928

FLOW STRUCTURE IN THE WAKE OF A WALL-MOUNTED BLUFF BODY

James H. J. Buchholz
IIHR - Hydroscience & Engineering,
Department of Mechanical
and Industrial Engineering
University of Iowa
Iowa City, IA 52242
Email: james-h-buchholz@uiowa.edu

Seyed Mohammad Hajimirzaie
IIHR Hydroscience & Engineering,
Department of Civil and
Environmental Engineering
University of Iowa
Iowa City, Iowa, 52242

Craig J. Wojcik
IIHR Hydroscience & Engineering,
Department of Mechanical
and Industrial Engineering
University of Iowa
Iowa City, Iowa, 52242

ABSTRACT

This paper discusses an experimental study of the flow field around three different wall-mounted obstacles in a boundary layer within a relatively shallow flow ($d/H \approx 4$, where d is the flow depth and H is the obstacle height). The first two obstacles consist of a semi-ellipsoidal body with the major axis of the base ellipse oriented in the streamwise and the transverse direction. The third obstacle is a low-aspect-ratio cylinder, bearing greater similarity to geometries investigated in other studies. Reynolds numbers of 5500 and 17800, based on obstacle height, were investigated. Digital particle image velocimetry was used to characterize the flow field in each case. At $Re_H = 17800$, isocontours of streamwise vorticity reveal the presence of a tip vortex pair and a base vortex pair for each geometry; however, the ratio of the relative strengths of the tip and base vortices varies considerably, with the streamwise-oriented ellipsoid having the largest ratio of tip/base vortex circulation and the transverse ellipsoid having the smallest ratio. The presence of a base vortex for such low-aspect-ratio obstacles is unexpected, and therefore we hypothesize that its existence is related to the small d/H. It is anticipated that variation of geometry and d/H will help to elucidate the role of the base vortex in the three-dimensional vortex structure of the wake.

1 Introduction

Flow over wall-mounted bodies of finite extent has been the subject of numerous investigations since the geometry is ubiquitous, appearing in a broad range of engineered and natural systems such as control surfaces, sails, and cowlings on submarines and aerodynamic vehicles; components on electronic circuit boards; buildings and exhaust stacks; and boulders, clusters, and fish habitat structures occurring on river beds. The simple geometry of a single wall-mounted obstacle in a boundary layer or channel (2-D or open) flow creates an extremely complex, highly three-dimensional and unsteady flow field for which the transport mechanisms of momentum and scalars are still not well-understood. Thus, details of the spatial shear stress distribution around these obstacles are also still not well understood (Martinuzzi and Tropea, 1993; Palau-Salvador et al., 2009). The wall-mounted obstacle is also the fundamental consituent of the very rough surfaces found in urban environments, and fluvial and ocean bottom boundary layers, and therefore it also plays an important role in the transport of scalars (e.g. Wang and McNamara (2007); Crimaldi et al. (2007)).

Because the flow is highly unsteady in the vicinity of these obstacles, the instantaneous velocities and stress distributions deviate significantly from the mean values, and thus the mean flow/Reynolds averaged flow description is of limited help in understanding the time evolution and structure of the instantaneous flow (Ballio et al., 1998; Vlachos and Hajj, 2002).

1.1 Flow structure around a wall-mounted obstacle

Fluid flow over wall-mounted obstacles has been studied extensively because of its ubiquity in natural and engineered systems. However, despite these efforts, there are many aspects that are still poorly understood due to the complexity of the resulting highly three-dimensional, unsteady flow and the sensitivity to a relatively large number of parameters that are required to describe this flow. Finite cylinders extending from a stationary wall

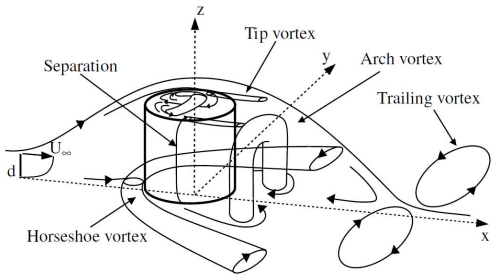

FIGURE 1. Three-dimensional vortex topology surrounding an obstacle at high relative submergence (from Pattenden et al. (2005).

(e.g. Pattenden et al. (2005); Sadeque et al. (2008, 2009); Palau-Salvador et al. (2009)) and prismatic obstacles (Martinuzzi and Tropea, 1993; Seal et al., 1995; Vlachos and Hajj, 2002) have been investigated most extensively; with fewer investigations of spherical bodies (e.g. Shamloo et al. (2001)) and other, more complicated geometries (e.g. Strom and Papanicolaou (2007)).

Figure 1 shows a recent interpretation by Pattenden et al. (2005) of the mean three-dimensional vortex topology surrounding a wall-mounted cylinder. The figure illustrates three dominant features which are qualitatively robust for different obstacle geometries: the horseshoe vortex wrapping around the body, the arch vortex in the near wake, and the tip vortices emerging from the free end. The dynamics of the horseshoe vortex upstream of the body have been studied extensively, and it is well-established that the horseshoe "system" may be comprised of several vortices evolving in a repetitive cycle of horseshoe vortex system formation, amalgamation, and decay (e.g. Baker (1979, 1980)). Complexity and unsteadiness in the horseshoe vortex has been found to increase with Reynolds number (Baker, 1979, 1980; Seal et al., 1995; Simpson, 2001). Several investigations reported the existence of a bimodal velocity probability distribution function in the junction region upstream of the body, associated with very large turbulent stresses (Devenport and Simpson, 1987a,b, 1990; Dargahi, 1989; Larousse et al., 1991; Martinuzzi and Tropea, 1993; Olçmen and Simpson, 1997). Devenport and Simpson (1990) attributed the behavior to the intermittent entrainment of low-momentum boundary layer structures in the corner region between the wall and leading edge. Seal et al. (1995) and Paik et al. (2007) demonstrated that the 'primary' vortex in the horseshoe vortex system (adjacent to the obstacle) is annihilated through the entrainment and mixing with opposite-sign vorticity lifted from the bed surface, and then replaced by the vortex advancing behind it. There has been little quantitative agreement in the literature about the relationship between flow parameters (e.g. Reynolds number) and the number of vortices present in the horseshoe system and their behavior, but most of the studies agree that the unsteadiness in the vortex system in front of the obstacle is independent of vortex shedding in the wake (Ballio et al., 1998; Wang and Zhou, 2009). However, Fu and Rockwell (2005); Rockwell (2008) showed that for very shallow flows there is interdependency between the horseshoe vortex oscillations upstream of the obstacle and vortex shedding in the wake.

In general, the behavior in the wake of the obstacle is markedly different from that of two-dimensional bluff bodies. Shedding behavior is highly three-dimensional at the tip of the structure where the tip vortices interact strongly with the shear-layer or Kármán vortices shed from the sides. Near the tip, vortex shedding is usually symmetric, and for sufficiently large aspect ratio H/D, the shedding mode may transition from the symmetric shedding near the tip to antisymmetric Kármán shedding near the base. However, there is not general agreement about the aspect ratio at which the transition first appears (Wang and Zhou, 2009). Obstacle shape has also been shown to have a significant effect on the flow structures and forces on the obstacle (Sousa and Pereira, 2004).

The wake also contains organized streamwise structures. As Figure 1 shows, the tip vortices and the legs of the horseshoe vortex are oriented primarily in the streamwise direction in the wake. Viewed in the streamwise direction, the tip and horseshoe structures form counter-rotating vortex pairs that are of the same sense, such that the tip structure descends toward the wall (Palau-Salvador et al., 2009). An additional streamwise structure not depicted in Figure 1 is the streamwise base vortex pair, located between the legs of the horseshoe but of opposite sign. It is usually observed for high aspect ratios (Sumner et al., 2004) or in boundary layers that are thick with respect to the obstacle height (Wang and Zhou, 2009). Sumner et al. (2004) observed a base vortex for H/D of 5, 7, and 9, but not for $H/D = 3$. They proposed that the base vortices may be time-averaged representations of the Kármán vortices and therefore would not be expected at the lowest aspect ratio where Kármán shedding is also expected to be suppressed. Wang and Zhou (2009) propose that the tip, base, and spanwise symmetric or Kármán vortices are all local manifestations of the same horseshoe-like structure shed in the wake, suggesting that the mean tip vortex structures shown in Figure 1 are actually much more complex in the instantaneous flow field.

The present work has been motivated by the need for an improved understanding of transport mechanisms in freshwater mussel populations. Freshwater mussels such as the Threeridge (Amblema plicata) shown in Figure 2 are filter feeders that live in rivers at the sediment-water interface, typically partially- to fully-embedded in the sediment. They are believed to have a significant effect on water quality since they collectively process very large volumes of water (T. Newton, USGS, personal communication). However, many native species have become endangered or extinct due to pollution, overharvesting, introduction of non-native invasive species, destruction of habitats (e.g. dredging and construction of locks and dams on the Mississippi River), and changes in land use patterns (Strayer et al., 2004). Freshwater mussels can exist in sparse distributions over the river bed, or in communities (mussel beds) where the density can reach 100 m^{-2}. Many factors are believed to contribute to habitat quality, including sediment type, and hydrodynamic factors governing transport of mussel larvae and juveniles, stability, and transport of nutrients and waste (Young, 2006). It is predicted that nutrient

(a) (b) (c)

FIGURE 2. Photographs of a Threeridge (Amblema plicata) mussel shell collected from Pool 16 of the Upper Mississippi River near Fairport, IA. (a) side view (flow left to right), (b) upstream-looking view, (c) top view (flow top to bottom).)

competition is a factor limiting mussel populations in all but the most sparsely-distributed communities (Morales et al., 2006).

The goals of this paper are two-fold. First, we wish to make a contribution to the understanding of hydrodynamic effects on mussel habitat quality, and therefore we investigate an idealized geometry that broadly represents the shape of a mussel protruding from the sediment. Whereas these benthic organisms exist in an open-channel environment, we consider here the case of a boundary layer flow. This approach is taken in order to simplify the flow field and provide a benchmark for further work. It will also facilitate comparison with previous work which has most often been conducted in boundary layer flows. Equally important, we want to make some fundamental contributions to the understanding of the flow field surrounding a surface-mounted obstacle, particularly focusing on the evolution of flow structure with variation in shape and flow parameters. As such, we consider not only the idealized mussel geometry, but also include measurements of flow over a low-aspect-ratio surface-mounted cylinder, which more closely represents geometries presented in the literature.

2 Method

Three geometries are investigated here. The first two represent a mussel in its usual (streamwise-aligned) orientation and oriented 90 degrees from the streamwise orientation to form a bluff body. The third geometry is a circular cylinder of aspect ratio $H/D = 0.56$ (where H = 50 mm is the cylinder height and D is the cylinder diameter. The mussel geometry is approximated as a semi-ellipsoid with primary axes obtained by measurement of more than 50 mussel shells representing 14 species. The mussels were collected in a quadrat in Pool 16 of the Mississippi River near Fairport, IA (Nakato et al., 2007). The dimensions of the major and minor axes of the base are 56 mm and 75 mm, and the height is 50 mm, as illustrated in Figure 3. Since mussels are embedded in the sediment, only half the ellipsoid is considered. All three geometrical configurations were investigated at

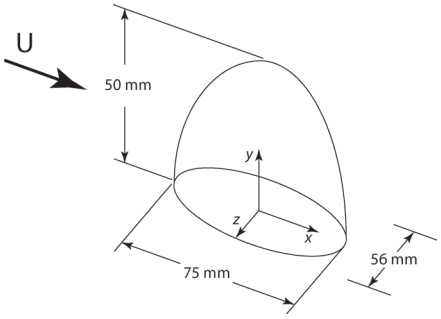

FIGURE 3. Coordinate system definition and idealized mussel geometry. The streamwise configuration is shown.

Reynolds numbers $Re_H = UH/\nu = 5500$ and 17800, where U is the freestream velocity.

Experiments were conducted in a water channel of width 0.6 m, depth 0.3 m, and length 10 m. The obstacle was mounted on a 12 mm thick flat acrylic plate and centered 152 mm from the leading edge of the plate. The plate leading edge was rounded and measurements of the flow in the vicinity of the leading edge verified that the flow over the leading edge was symmetric with the stagnation point on the center of the rounded edge and that there was no flow separation. The flow depth was d = 195 mm above the plate, and a second plate of the same dimensions constrained the free surface in order to remove free-surface-related flow effects and to enable optical interrogation.

Digital Particle Image Velocimetry (DPIV) (Willert and Gharib, 1991; Raffel et al., 2007) was used to characterize freestream flow characteristics, boundary layer characteristics on the plate in the absence of the obstacle, and the highly three-dimensional, unsteady flow surrounding the obstacle. A LaVision Inc. Flowmaster system was employed, consisting of a 2048×2048 pixel interline transfer CCD camera with 14-bit dynamic range; a dual-cavity, 200 mJ/pulse Nd:YAG laser with light sheet optics, and a PC-based timing and data acquisition system managed by LaVision DaVis 7.2 software. Standard cross-correlation analysis was employed in multiple passes on window sizes of 64×64 pixels and 32×32 pixels with 50% overlap. A local median filter was used to eliminate outliers. DPIV data were acquired in two orthogonal planes. The first location focused on the separated region downstream of the obstacle on the symmetry ($z = 0$) plane. In the second case, the laser sheet was oriented in the y-z plane at $x = 75$ mm.

3 Results

In the absence of obstacles, a boundary layer of thickness $\delta_{99} \approx 10$ mm was present on the plate at the location of the obstacle center. Thus for each of the three geometries, the relative boundary thickness $\delta_{99}/H \approx 0.2$. An additional boundary layer existed on the top plate constraining the free surface. The mean streamwise velocity measured 30 cm upstream of the plate leading edge was uniform within 1% and the maximum turbulence intensity was approximately 5% in the low-Reynolds-

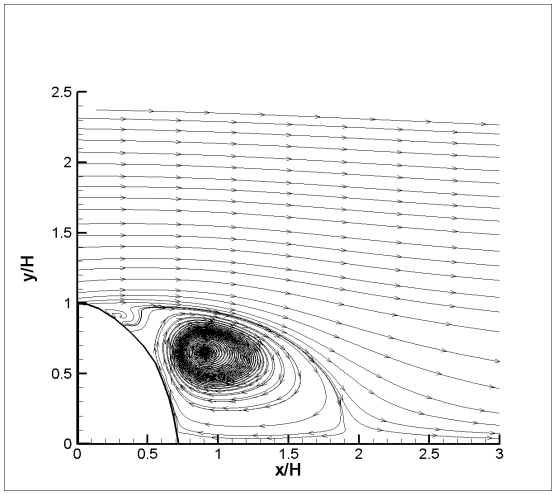

(a)

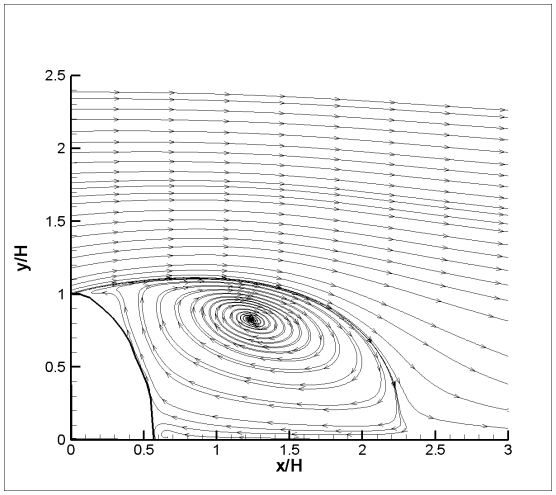

(b)

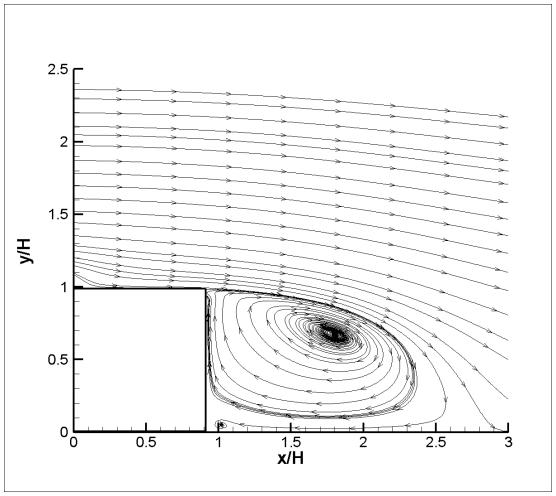

(c)

FIGURE 4. Mean streamlines downstream of the obstacle at $Re_H = 5500$. (a) Streamwise-oriented ellipsoid, (b) transversely-oriented ellipsoid, and (c) cylinder.

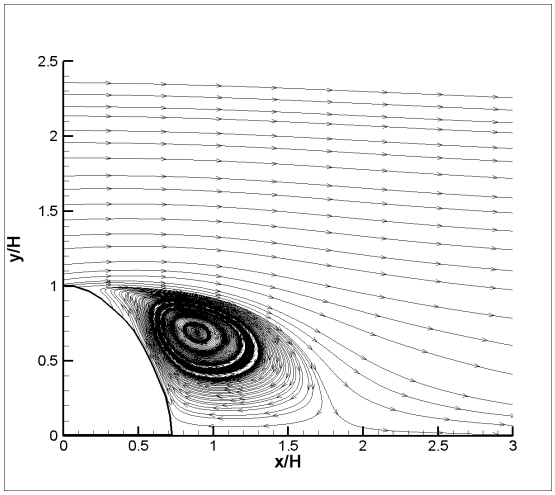

(a)

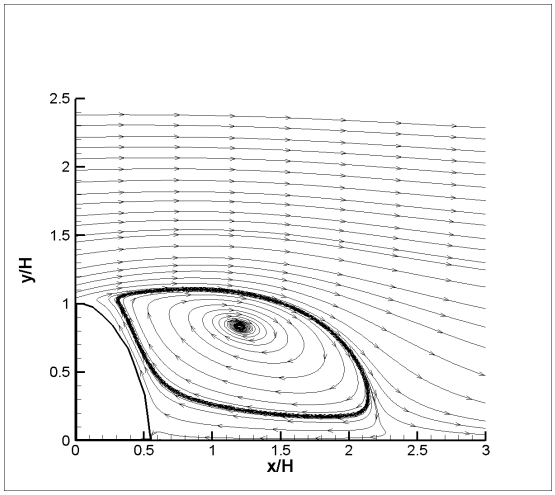

(b)

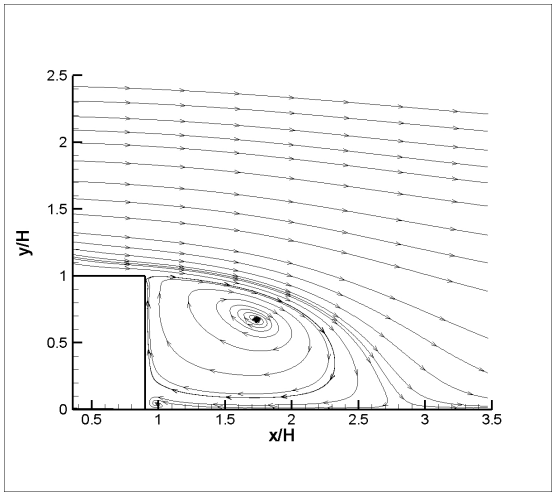

(c)

FIGURE 5. Mean streamlines downstream of the obstacle at $Re_H = 17800$. (a) Streamwise-oriented ellipsoid, (b) transversely-oriented ellipsoid, and (c) cylinder.

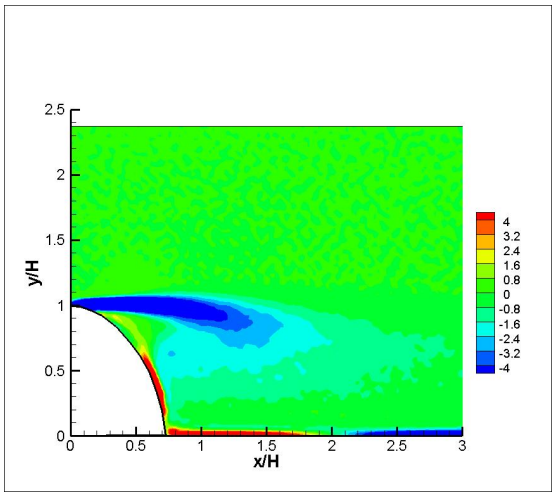

(a)

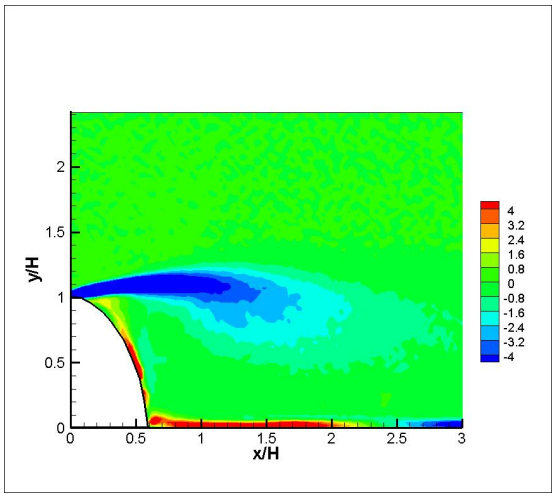

(b)

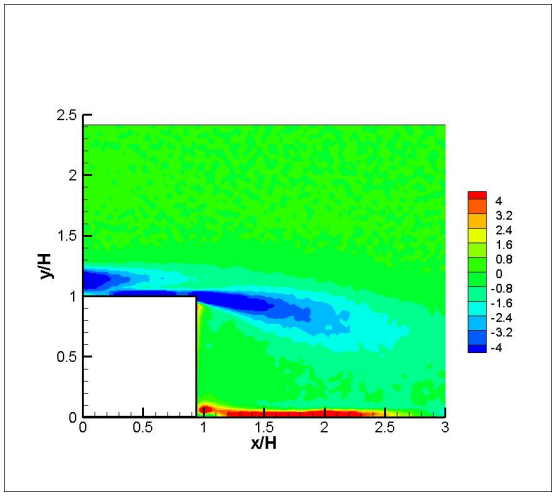

(c)

FIGURE 6. Isocontours of nondimensional spanwise vorticity downstream of the obstacle at $Re_H = 5500$. (a) Streamwise-oriented ellipsoid, (b) transversely-oriented ellipsoid, and (c) cylinder. Red shades indicate counter-clockwise rotation and blue shades indicate clockwise rotation.

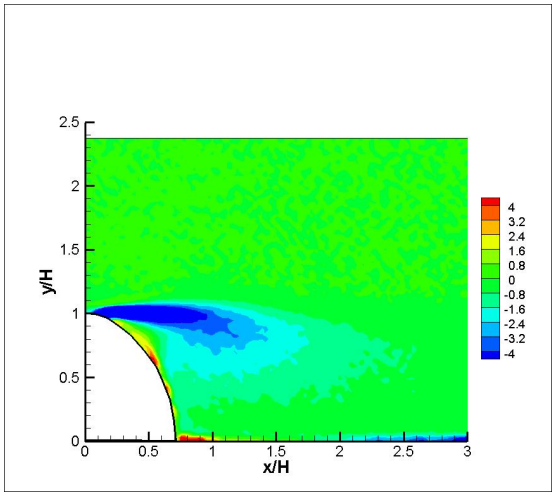

(a)

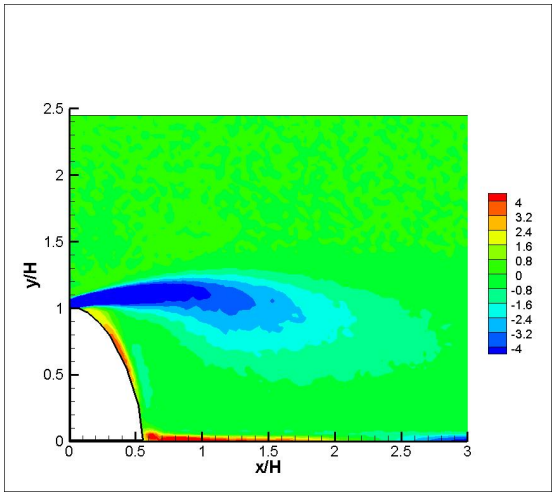

(b)

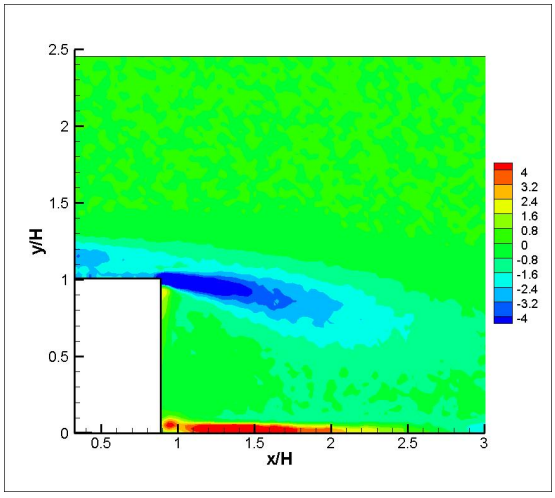

(c)

FIGURE 7. Isocontours of nondimensional spanwise vorticity downstream of the obstacle at $Re_H = 17800$. (a) Streamwise-oriented ellipsoid, (b) transversely-oriented ellipsoid, and (c) cylinder. Red shades indicate counter-clockwise rotation and blue shades indicate clockwise rotation.

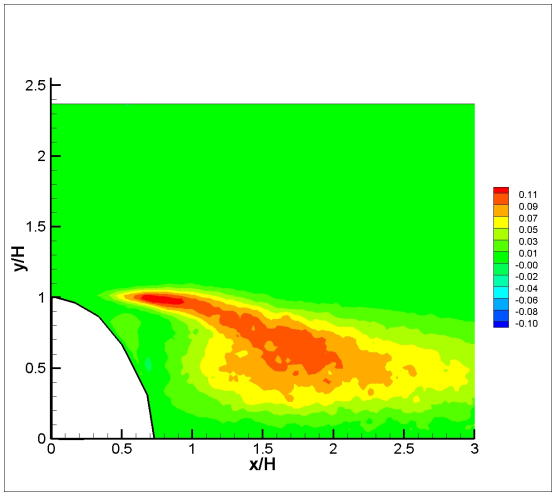

(a)

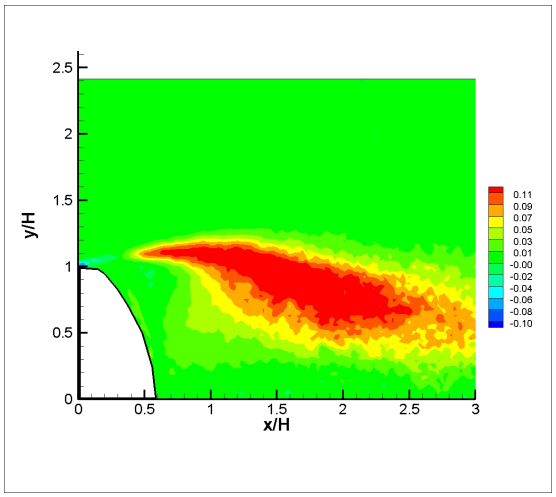

(b)

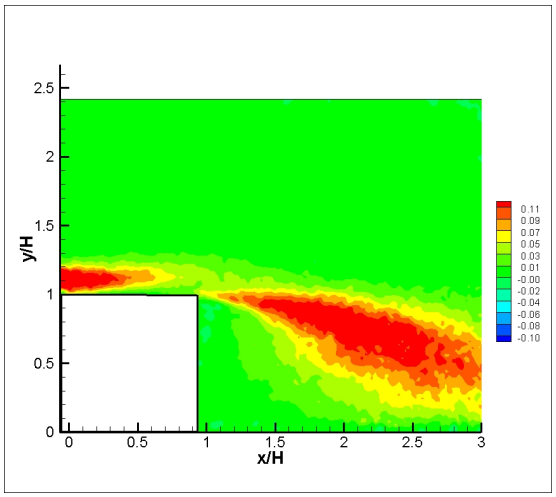

(c)

FIGURE 8. Isocontours of Reynolds shear stress $-\overline{u'v'}/U^2$ downstream of the obstacle at $Re_H = 5500$. (a) Streamwise-oriented ellipsoid, (b) transversely-oriented ellipsoid, and (c) cylinder.

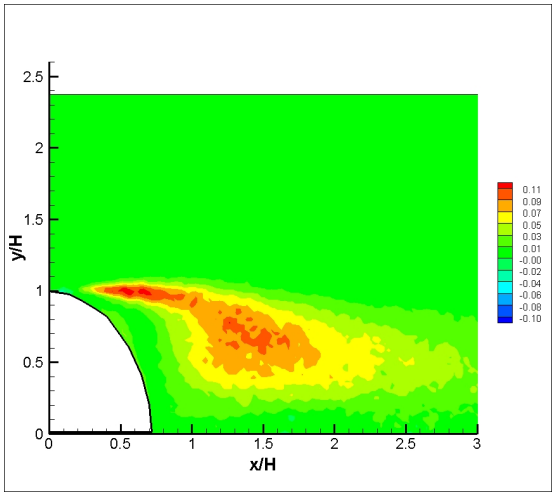

(a)

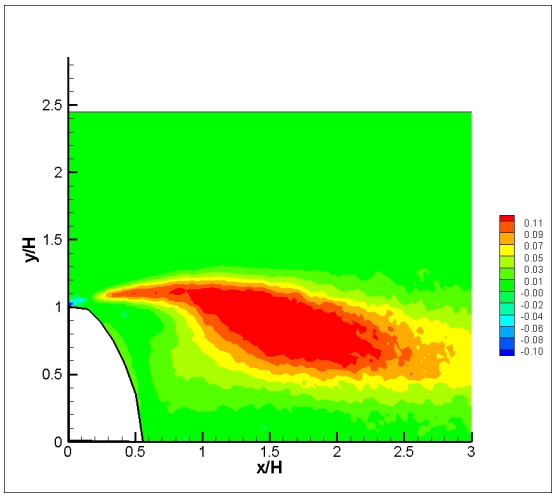

(b)

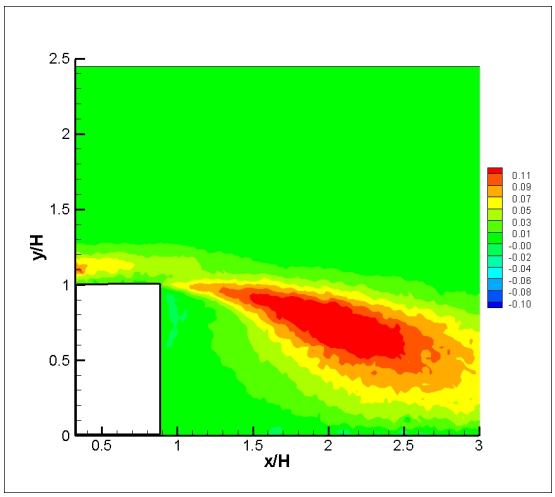

(c)

FIGURE 9. Isocontours of Reynolds shear stress $-\overline{u'v'}/U^2$ downstream of the obstacle at $Re_H = 17800$. (a) Streamwise-oriented ellipsoid, (b) transversely-oriented ellipsoid, and (c) cylinder.

Obstacle	x_r/H	$(x_r - x_{t.e.})/H$
Low Re		
Streamwise	2.0	1.44
Transverse	2.48	1.73
Cylinder	2.83	1.94
High Re		
Streamwise	1.9	1.34
Transverse	2.41	1.66
Cylinder	2.75	1.86

TABLE 1. Mean dimensionless reattachment lengths on the symmetry plane measured from the obstacle center line (x_r/H) and the trailing edge ($(x_r - x_{t.e.})/H$).

number case, and 7% at high Reynolds number. At $Re_H = 5500$, the boundary layer displacement thickness and momentum thicknesses were $\delta^* = 1.5$ mm and $\theta = 0.77$ mm, providing a shape factor of 2.01. At $Re_H = 17800$, $\delta^* = 0.94$ mm, $\theta = 0.66$ mm, and $H = 1.44$. Despite the relatively low boundary layer Reynolds numbers – $Re_x \approx 17000$ and 54000 – the profiles are not very representative of a Blasius profile ($H = 2.59$), likely due to the relatively high freestream turbulence intensities.

3.1 Time-averaged Quantities on the Symmetry Plane

Figures 4 and 5 contain the mean streamlines each obtained from 2000 velocity fields downstream of the three geometries at $Re_H = 5500$ and $Re_H = 17800$, respectively. Table 1 contains the reattachment lengths on the symmetry plane measured from the center of the obstacle, and from the obstacle trailing edge, and non-dimensionalized by the obstacle height. The effect of Reynolds number on reattachment length is not significant within the range considered here. The greatest variation with Reynolds number was found for the streamwise ellipsoid which, when measured from the trailing edge, varies by only 7%. The cylinder is the most blunt of the three geometries and has the longest reattachment length. Measured from the trailing edge, the cylinder reattachment length is approximately 35% greater than the streamwise ellipsoid at $Re_H = 5500$, and 39% greater at $Re_H = 17800$. The reattachment lengths for the transverse ellipsoid fall between these extreme cases at both Reynolds numbers.

Isocontours of nondimensional spanwise vorticity ($\omega_z H/U$) are shown in Figures 6 and 7 for the low- and high-Reynolds-number conditions, respectively. The regions of large negative ω_z (counter clockwise rotation) are located in the vicinity of the separated shear layer downstream of the obstacle. Significant positive vorticity is found for each geometry adjacent to the base plane in the vicinity of the recirculation region. Large positive values also exist on the lee faces of the streamwise and transverse ellipsoids. It is evident from both the streamline (Figures 4 and 5) and vorticity (Figures 6 and7) plots that the flow rising on the lee surface of the ellipsoids encounters an adverse pressure gradient. This is suggested by the diffusion of the surface adjacent vorticity with increasing vertical distance along the ellipsoid perimeter and, for $Re_H = 5500$, flow separation.

The distributions of kinematic Reynolds shear stress ($-\overline{u'v'}/U^2$) in the wake of the obstacles is shown in Figures 8 and 9 for the low and high Reynolds numbers, respectively. The lowest magnitudes occur for the streamwise ellipsoid. There is a fundamental difference between the flow field over the two ellipsoids and that over the cylinder. On the symmetry plane, the cylinder has separation points on the top surface at the leading and trailing edges. The separated shear layer of the first separation transitions to turbulence before reattaching, and therefore there is higher turbulence intensity in the flow at the second separation point. In contrast, for the ellipsoids, there is only one separation point, near the top of the structure, and therefore the Reynolds stresses are significantly lower just after separation. For the ellipsoids, isocontours of large value are found nearer the separation point in the high Reynolds number conditions than in low Reynolds number conditions, consistent with the expectation that transition would occur sooner in the separated shear layer at higher Reynolds number. Given that freshwater mussels are expected to position themselves in the streamwise orientation, the lower wake turbulence levels could result in reduced transport of nutrients and waste within the benthic boundary layer in comparison to cylindrical or prismatic bodies.

3.1.1 Streamwise Vorticity and Circulation

Figure 10 contains isocontours of non-dimensional streamwise vorticity $\omega^* = \omega H/U$ in a transverse $(y-z)$ plane located at $x/H = 1.5$, at $Re_H = 17800$ for the three geometries. Each mean vorticity field was obtained from 3000 instantaneous velocity fields. These figures focus on the inner portion of the wake – the cores of the mean horseshoe structures can be observed at the left and right edges of Figure 10(a), and fall outside of the field of view in the other two cases. In all three cases, a tip vortex pair and base vortex pair are evident; however, the relative strengths vary significantly between the three cases. The presence of the base vortex is unexpected due to the very low aspect ratio of these obstacles. The cylinder diameter is larger than the cross-sectional dimensions of the ellipsoid, and has a broader wake such that the right side of the vorticity isocontours are truncated in the image. However, in this case a weak, tertiary vortex pair of the same sign as the tip vortex, is observed near the base plane.

The circulation of each of the identified structures was computed using the method of Buchholz and Smits (2008) within an isocontour of $\omega^* = 0.07$. The non-dimensional circulation $\Gamma^* = \Gamma/(UH)$ was calculated for each vortex in the tip, base, and (for the cylinder) tertiary structures. The results are given in Table 2. The deviation $\delta\Gamma^* = (|\Gamma^*_L - \Gamma^*_R|)/(2|\overline{\Gamma^*}|) \times 100\%$ is also given, where Γ^*_L and Γ^*_R are the circulations of the left- and right-vortices in the pair, respectively. For the cylinder, the values were determined using only the left side of each pair. The tip vortex pair is dominant in the wake of the streamwise ellip-

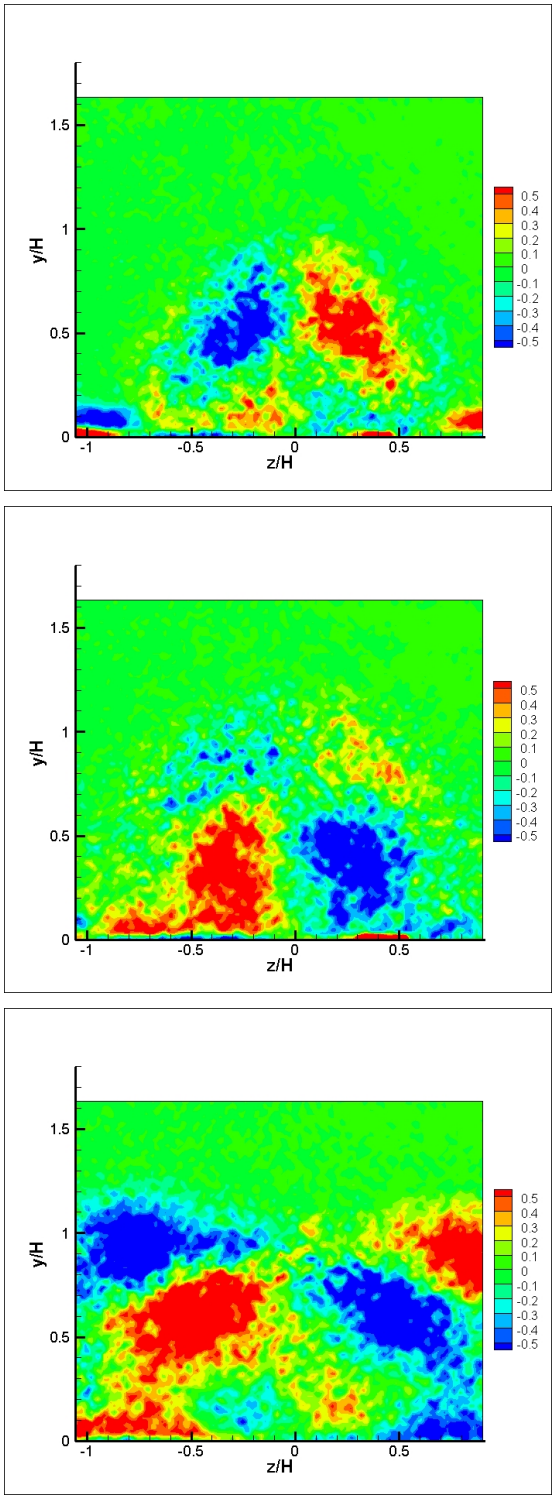

FIGURE 10. Isocontours of non-dimensional streamwise vorticity in the plane $x/H = 1.5$ for the case $Re_H = 17800$. (a) streamwise-oriented ellipsoid, (b) transversely-oriented ellipsoid, (c) cylinder. Red shades indicate counter-clockwise rotation and blue shades indicate clockwise rotation.

Obstacle	Structure	$\lvert\overline{\Gamma^*}\rvert$	$\delta\Gamma^*$ (%)
Streamwise			
	tip	0.101	1.3
	base	0.0301	16
Transverse			
	tip	0.0416	19
	base	0.167	0.4
Cylinder			
	tip	0.161	–
	base	0.250	–
	tertiary	0.0149	–

TABLE 2. Average dimensionless circulations of structures identified in Figure 10, and the left/right deviation.

soid; however, the base vortex pair is dominant in the transverse ellipsoid. In the wake of the cylinder, the strengths are more balanced but the base vortex is stronger, as with the transverse ellipsoid. The vorticity field in the wake of the cylinder is particularly surprising since base vortices are typically found to occur only for much larger aspect ratios (Sumner et al., 2004). At such low aspect ratio, the tip and base vortices are necessarily in close proximity and appear to interact strongly, presumably driving a rapid transverse expansion in the wake. To the authors' knowledge, this is the first time a tertiary structure has been observed in a finite cylinder wake. It may have been generated on the base plane due to the interaction of a strong base vortex with the base plane.

4 Discussion

In the present experiments, the obstacle height is approximately 25 % of the flow depth, and for the cylinder (the largest obstacle), the blockage is approximately 4%. In the context of open channel flow Shamloo et al. (2001) has identified four flow regimes corresponding to variation in relative submergence d/h, where d is the flow depth and h is the characteristic obstacle length scale (e.g. the obstacle height). Whereas for $d/h > 4$, the presence of the obstacle left no discernable signature on the free surface and flow patterns were qualitatively consistent with those observed around obstacles immersed in boundary layer flows; for $d/h < 1$, standing waves formed around the obstacle, and a Kármán vortex street was reported in the wake. A similar phenomenon occurs in stratified atmospheric flows around islands (Smith and Grubišić, 1993). While the classifications of Shamloo et al. delineate flow regimes with significant physical distinctions, they are not sensitive to more subtle variations in the flow field that may occur as d/h approaches 4 from above. Given that, in the literature, the base vortex is generally not observed for

low-aspect-ratio obstacles, we surmise that its existence here is related to the limited depth. The presence of the base vortex and the concurrent transverse spreading of the near wake that would be expected from the vortex interactions here may be due to the relatively shallow depth of the flow, causing more flow to be deflected around the obstacle instead of over it.

For $Re_H = 5500$, we examined the effect of relative submergence (d/H) by descending the top plate until it touched the tip of the transverse ellipsoid, and visualized the flow using fluorescein dye injected from ports on the upstream face of the obstacle. The results are shown in Figure 11. While at high relative submergence, we see a broad, symmetric wake expected for such a low-aspect-ratio geometry; at low relative submergence, antisymmetric shedding and a sinuous wake are clearly visible. These results are qualitatively in agreement with the consensus in the literature, which reports the absence of Kármán shedding in the wakes of deeply-submerged low-aspect-ratio obstacles, and the existence of Kármán shedding behind low-aspect-ratio obstacles in shallow flows ($d/h \lessapprox 1$). The streamwise vorticity distribution, with strong base vortex, shown in Figure 10(b) corresponds to the same geometry as Figure 11(a). The Reynolds numbers are different between the two cases; however, if the qualitative flow pattern of Figure 11(a) is relevant to the flow at $Re_H = 17800$, then the data presented here would suggest that the base vortex is not a projection of Kármán vortices as suggested by Sumner et al. (2004), since their existence is not apparent.

It is anticipated that the presence of the base vortex will have an effect on vertical transport of scalars and momentum in the wakes of the bodies investigated here. Assuming that the presence of the base vortex is related to the low relative submergence, this may enhance mixing of nutrients and waste for mussel communities existing in shallow flows. It may also have some adverse effect on the stability of sediments within mussel communities, perhaps influencing, among other factors (e.g. temperature, protection from predators, reduced susceptibility to water level variations), their selection of flow depth.

From the data presented here, it is not clear how the base vortex might fit into a three-dimensional vortex skeleton model of the wake. From observations of the instantaneous streamwise vorticity field at $x/H = 1.5$, a coherent base vortex cannot be identified - as in Pattenden et al. (2005), the instantaneous vorticity field in the wake tends to be highly incoherent. Therefore, it is not clear whether the base (and tip) vortices here are quasi-stationary, as in the case of a wing tip vortex, or whether they are simply averages of many individual shed structures as in the model of Wang and Zhou (2009). We suspect the latter; however, the connectivity would likely be complex given the significant differences in circulation between the tip and base vortices in each case.

5 Conclusions

The flow field surrounding a wall-mounted cylinder and ellipsoid was investigated for $Re_H = 5500$ and 17800. The obstacles had low aspect ratios ($H/D < 1$) and were studied in a flow

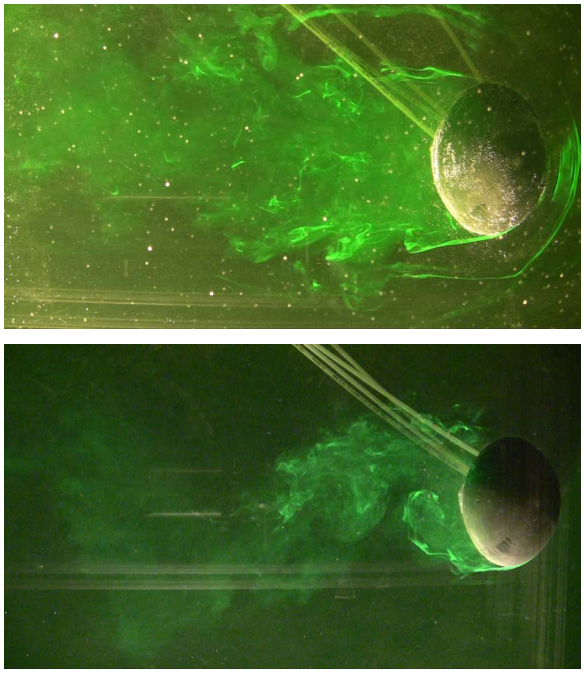

FIGURE 11. Dye visualizations of the flow around the transversely-oriented ellipsoid at $Re_H = 5500$. (a) $d/H \approx 4$, (b) $d/H = 1$.

of low relative submergence. At both Reynolds numbers, the mean flow in the symmetry plane of the ellipsoid oriented in the streamwise and transverse positions exhibited a laminar separation near the top of the structure, which transitioned to turbulence and reattached to the base plane downstream of the obstacle. The streamwise ellipsoid had the shortest reattachment length of the three geometries and the lowest Reynolds shear stresses on the symmetry plane.

A base vortex was observed in each case, in contrast to observations reported in the literature for flows over low-aspect-ratio obstacles at higher relative submergence. It is hypothesized here that this anomaly is due to interference caused by the the low value of $d/H \approx 4$ which causes a preferential redirection of flow around the obstacle rather than over it. Further investigation is needed to understand the role of the base vortex in the three-dimensional vortex skeleton in the wake of these bluff bodies; however, it is expected that further work in which the strengths of the tip and base structures are controlled by variation in geometry and relative submergence will provide valuable insights into this question.

6 Acknowledgements

The authors thank Dr. N. Young (IIHR - Hydroscience & Engineering, University of Iowa) and Dr. T. Newton (USGS) for sharing their knowledge on mussel hydrodynamics and habitats. Mr. P. Haug and the late Mr. H. Dircks are thanked for their assistance with facilities and model construction.

REFERENCES

C. J. Baker. The laminar horseshoe vortex. *J. Fluid Mech.*, 95 (2):347–367, 1979.

C. J. Baker. The turbulent horseshoe vortex. *J. Wind Eng. Ind. Aerodyn.*, 6:9–23, 1980.

F. Ballio, C. Bettoni, and S. Franzetti. A survey of time-averaged characteristics of laminar and turbulent horseshoe vortices. *ASME J. Fluids Eng.*, 120:233–242, 1998.

J. H. J. Buchholz and A. J. Smits. The wake structure and thrust performance of a rigid low-aspect-ratio pitching panel. *J. Fluid Mech.*, 603:331–365, 2008.

J. P. Crimaldi, J. R. Koseff, and S. G. Monismith. Structure of mass and momentum fields over a model aggregation of benthic filter feeders. *"Biogeosciences"*, 4:269–282, 2007.

B. Dargahi. The turbulent flow field around a circular cylinder. *Exp. Fluids*, 8:1–12, 1989.

W. J. Devenport and R. L. Simpson. Some time-dependent features of turbulent appendage-body junction flows. In *The 16th Symposium on Naval Hydrodynamics*, pages 312–335, Berkeley, CA, 1987a.

W. J. Devenport and R. L. Simpson. Turbulent structure near the nose of a wing-body junction. AIAA Paper 87-1310, 1987b.

W. J. Devenport and R. L. Simpson. Time-dependent and time-averaged turbulence structure near the nose of a wing-body junction. *J. Fluid Mech.*, 210:23–55, 1990.

H. Fu and D. Rockwell. Shallow flow past a cylinder: Transition phenomena at low reynolds number. *J. Fluid Mech.*, 540:75–97, 2005.

A. Larousse, R. Martinuzzi, and C. Tropea. Flow around surface-mounted, three-dimensional obstacles. In *Turbulent Shear Flows 8; Eighth Int. Symp. on Turbulent Shear Flows*, Munich, Germany, 1991. Springer-Verlag.

R. Martinuzzi and C. Tropea. The flow around surface-mounted, prismatic obstacles placed in a fully developed channel flow. *ASME J. Fluids Eng.*, 115:85–92, 1993.

Y. Morales, L. J. Weber, A. E. Mynett, and T. J. Newton. Mussel dynamics model: A hydroinformatics tool for analyzing the effects of different stressors on the dynamics of freshwater mussel communities. *Ecol. Model.*, 197:448–460, 2006.

T. Nakato, J. Christensen, and B. Schonhoff. Freshwater mussel survey in pool 16, the mississippi river, near fairport, iowa: R.m. 463.5 - r.m. 464.1, approximately. IIHR Technical Report 464, The University of Iowa, IIHR - Hydroscience & Engineering, August 2007.

O. Olçmen and R. L. Simpson. Some features of a turbulent wing-body junction vortical flow. AIAA Paper 97-0651, 1997.

J. Paik, C. Escauriaza, and F. Sotiropoulos. On the bimodal dynamics of the turbulent horseshoe vortex system in a wing-body junction. *Phys. Fluids*, 19, 2007. Art. 045107.

G. Palau-Salvador, T. Stoesser, J. Fröhlich, M. Kappler, and W. Rodi. Large eddy simulations and experiments of flow around finite-height cylinders. *Flow Turbulence Combust.*, 84 (2):239–275, 2009.

R. J. Pattenden, S. R. Turnock, and Z. Zhang. Measurements of the flow over a low-aspect-ratio cylinder mounted on a ground plane. *Exp. Fluids*, 39:10–21, 2005.

M. Raffel, C. Willert, S. T. Wereley, and J. Kompenhans. *Particle Image Velocimetry: A Practical Guide*. Springer, Berlin, 2 edition, 2007.

D. Rockwell. Vortex formation in shallow flows. *Phys. Fluids*, 20, 2008. Art. 031303.

M. A. F. Sadeque, N. Rajaratnam, and M. R. Loewen. Flow around cylinders in open channels. *J. Eng. Mech.*, 134(1):60–71, 2008.

M. A. F. Sadeque, N. Rajaratnam, and M. R. Loewen. Effects of bed roughness on flow around bed-mounted cylinders in open channels. *J. Eng. Mech.*, 135(2):100–110, 2009.

C. V. Seal, C. R. Smit, O. Akin, and D. Rockwell. Quantitative characteristics of a laminar, unsteady necklace vortex system at a rectangular block - flat plate juncture. *J. Fluid Mech.*, 286: 117–135, 1995.

H. Shamloo, N. Rajaratman, and C. Katopodis. Hydraulics of simple habitat structures. *J. Hydraulic Res.*, 39(4):351–366, 2001.

R. L. Simpson. Junction flows. *Annu. Rev. Fluid Mech.*, 33: 415–443, 2001.

R. B. Smith and V. Grubišić. Aerial observations of hawaii's wake. *J. Atmos. Sci.*, 50(22):3728–3750, 1993.

J. M. M. Sousa and J. C. F. Pereira. DPIV study of the effect of a gable roof on teh flow structure around a surface-mounted cubic obstacle. *Exp. Fluids*, 37:409–418, 2004.

D. L. Strayer, J. A. Downing, W. R. Haag, T. L. King, J. B. Layzer, T. J. Newton, and S. J. Nichols. Changing perspectives on pearly mussels, north america's most imperiled animals. *BioScience*, 54(5):429–439, 2004.

K. Strom and A. Papanicolaou. ADV measurements around a cluster microform in a shallow mountain stream. *J. Hydraulic Eng.*, 133(12):1379–1389, 2007.

D. Sumner, J. L. Heseltine, and O. J. P. Dansereau. Wake structure of a finite circular cylinder of small aspect ratio. *Exp. Fluids*, 37:720–730, 2004.

P. P. Vlachos and M. R. Hajj. A time-resolved DPIV study of the unsteady character of the flow over a surface-mounted prism. *J. Wind Eng. Ind. Aerodyn.*, 90:543–553, 2002.

H. F. Wang and Y. Zhou. The finite-length square cylinder near wake. *J. Fluid Mech.*, 638:453–490, 2009.

X. Wang and K. F. McNamara. Effects of street orientation on dispersion at or near urban street intersections. *J. Wind Eng. Ind. Aerodyn.*, 95:1526–1540, 2007.

C. E. Willert and M. Gharib. Digital particle image velocimetry. *Exp. Fluids*, 10:181–193, 1991.

N. C. Young. *Physical Characterization of Freshwater Mussel Habitats in Upper Mississippi River Pool 16*. PhD thesis, University of Iowa, 2006.